

**ELIMINATION OF PESTICIDE ATRAZINE BY
PHOTOELECTROCATALYSIS USING A PHOTOANODE BASED ON WO₃
NANOSHEETS**

Fernández-Domene, R.M.^a; Sánchez-Tovar, R.^a; Lucas-granados, B.^a; Muñoz-Portero, M.J.^a; García-Antón, J.^{a*}

^aIngeniería Electroquímica y Corrosión (IEC). Departamento de Ingeniería Química y Nuclear. ETSI Industriales. Universitat Politècnica de València. Camino de Vera s/n, 46022 Valencia, Spain.

The photoelectrocatalytic (PEC) degradation of a persistent and toxic herbicide, atrazine, has been investigated by using a novel and high-performance WO₃ nanostructure in the form of nanosheets/nanorods as photoanode. The nanostructure has been synthesized by anodization in acidic media in the presence of a very small amount (0.05 M) of H₂O₂, and its morphology, as well as its electrochemical and photoelectrochemical properties have been characterized. Atrazine was completely degraded after ~180 minutes of reaction following pseudo-first order kinetics, and 2-hydroxyatrazine was identified as the main intermediate species. Moreover, the s-triazine ring in cyanuric acid (the final intermediate of atrazine degradation and very stable) was partially broken according to the obtained results, indicating the excellent PEC behavior of this WO₃ nanostructure.

KEYWORDS: WO₃ nanostructures; anodization; photoelectrocatalysis; atrazine degradation.

1. INTRODUCTION

The quality of human consumption water (for drinking, domestic purposes, food production, etc.) is fundamental for our daily life, due to the enormous impact it has on health. Because of that, drinking-water quality is one of the uppermost priorities of the World Health Organization [1]. However, according to the United Nations, 663 million people still use unimproved drinking water sources and more than the 40% of people in the world are affected by water scarcity, a percentage that could increase in the next years [1, 2]. This problem is aggravated by anthropogenic contamination of water resources with organic chemicals from agriculture and farming (fertilizers, pesticides...), chemical and pharmaceutical industry, urban wastewater, etc.

Pesticides, which are chemical compounds used to kill or control agricultural pests that would otherwise negatively affect the productivity of crops, have had a fundamental role in increasing food production, both quantitative and qualitatively, during the XX century. Unfortunately, along with these benefits, many environmental and health problems have also come, some of them so serious as to threaten the long-term survival of major ecosystems by loss of biodiversity, as well as human safety [3]. Many of the most effective pesticides are at the same time the most toxic and persistent and, when released to the environment, they can be transported overland and through the soil by irrigation, rainwater and melting snow, eventually finding their way into groundwater, wetlands, rivers, lakes and oceans [4]. In fact, pesticide concentrations measured in surface water and groundwater in many countries have exceeded the national drinking water limits [5-11], with the corresponding ecological impact on the life of plants and animals, including human beings [4, 9].

Atrazine is a triazine herbicide broadly used to control weeds in corn fields. It has been found to be very toxic to aquatic life with long lasting effects [9, 12-14]. Atrazine affects the reproduction of aquatic flora and fauna [9] and can act as an endocrine disruptor, as well as alter the reproductive systems or organs of animals [15, 16] and induce reproductive cancers in humans [17]. Since atrazine is very persistent (its half-life under natural light is very long, around 250 days [18]), it can be carried by surface runoffs to surface and groundwater reservoirs far away from the source of pollution. Due to all these negative aspects of atrazine, it was banned in the European Union in 2004, although in several communitarian countries the prohibition of atrazine was postponed until 2007 [19]. However, in many countries, such as USA, it is still in use [20].

Several techniques have been used to eliminate atrazine from aqueous solutions. Since conventional water treatment processes are not effective to eliminate this kind of persistent organic pollutants [18, 21, 22], advanced oxidation processes (AOPs) have been usually employed for those purposes, whose principle is the formation of the highly oxidant hydroxyl radicals, which can efficiently oxidize organic molecules. Among these processes, atrazine has been degraded using Fenton, photo-Fenton and electro-Fenton [23-30], ozonation with UV [24, 31], photolysis [18, 32-36], electrochemical oxidation [18, 23, 28-30, 34, 37] and photocatalysis [18, 22, 26, 30, 32, 35, 38-47]. Photoelectrocatalysis (PEC), which combines both electrochemistry and photocatalysis, has emerged as a potent tool to eliminate recalcitrant organic compounds in wastewater. PEC processes have several advantages over other AOPs: they require little to no reagents, hence minimizing the costs associated with additional treatments, and their operation is quite simple [18]. Besides, the fast recombination of

photogenerated electron-hole pairs which takes place in photocatalysis is greatly reduced or avoided by applying a small potential polarization to the photoanode, increasing significantly the efficiency of the process by extending the lifetime of holes for the production of hydroxyl radicals [18, 48, 49]. However, in spite of the promising results obtained by using PEC for the removal of several organic pollutants, this method has been rarely employed to eliminate atrazine from aqueous solutions [18, 34, 50], and these studies have all been carried out using TiO_2 as semiconductor material for the photoanode. In this work, the photoelectrochemical degradation of atrazine has been successfully achieved by using high-performance WO_3 nanosheets. WO_3 has a narrower bandgap than TiO_2 (2.6 eV vs. 3.1-3.2 eV), which makes it capable of absorbing in the blue region of the visible spectrum [51, 52]. Moreover, in contrast with almost the rest of semiconductor oxides used as photocatalysts, WO_3 can safely operate in acidic environments, which is very useful in the treatment of low-pH wastewater.

The objective of this study is to prove the excellent performance of a novel WO_3 nanostructure synthesized by anodization and with very high electroactive surface area for the degradation of the harmful pesticide atrazine. Previous to the photoelectrocatalytic tests, the morphological, electrochemical and photoelectrochemical properties of these WO_3 photoelectrodes have been characterized.

2. EXPERIMENTAL PROCEDURE

2.1 Reagents and materials

Atrazine and their intermediates were supplied by Sigma-Aldrich (Pestanal, analytical standard). The different stock aqueous solutions were prepared by dissolving the solid reagents for 24 h under vigorous magnetic stirring and then stored in the dark at 4 °C until use. These stock solutions were subsequently diluted to attain the desired concentrations.

The WO₃ nanostructures used in the PEC degradation experiments were synthesized by electrochemical anodization of tungsten cylinders of 8 mm in diameter, in an electrolyte of 1.5M H₂SO₄ + 0.05M H₂O₂ [53]. Before anodization, tungsten samples were wet abraded using 220-4000 grit SiC papers, rinsed with distilled water and ethanol and dried in an air stream. Afterward, tungsten cylinders were covered with a polytetrafluoroethylene (PTFE) coating to expose an area of 0.5 cm² to the electrolyte. Samples were anodized for 4 h, at 20 V and at 50 °C, under hydrodynamic conditions using a rotating disk electrode (at 375 rpm) and with a platinum mesh acting as the cathode of the cell. A WO₃ compact layer was also fabricated in order to compare its electrochemical and photoelectrochemical behavior with that of the WO₃ nanostructure. The compact layer was synthesized by anodization of the same tungsten cylinders in a peroxide-free electrolyte (1.5M H₂SO₄) at room temperature, imposing 20 V for 4 h. After anodization, the formed nanostructures and the compact layer were annealed using a tubular oven for 4 h at 400 °C.

2.2. Morphological and structural characterization of the WO₃ nanostructure

Morphological characterization of the obtained nanostructure was performed by Field Emission Scanning Electron Microscopy (FESEM), using a voltage of 3 kV.

The samples were examined by Confocal Raman Spectroscopy using a Witec Raman Confocal Microscope, before and after the heat treatment (annealing), in order to evaluate their crystalline structure. For these measurements, samples were illuminated with a 632 nm neon laser using 420 μ W. Energy Dispersive X-ray spectroscopy (EDX) was also used to verify the chemical composition of the WO_3 nanostructures, applying an accelerating voltage of 20 kV.

2.3. Electrochemical and photoelectrochemical characterization of the WO_3 nanostructure

All electrochemical and photoelectrochemical measurements were carried out using an Autolab PGSTAT302N potentiostat and a three-electrode electrochemical cell, with a Ag/AgCl 3M KCl reference electrode and a platinum wire counter electrode.

Cyclic voltammetry of the samples was performed in a 10 mM $\text{Fe}(\text{CN})_6\text{K}_4$ + 0.1 M H_2SO_4 solution, in the range potential between 0.15 and 0.6 V at 10 mV s^{-1} . Electrochemical impedance spectroscopy (EIS) measurements were performed in a 0.1 M H_2SO_4 electrolyte, at an applied potential of 0.7 V, using a potential perturbation amplitude of 10 mV and in the frequency range of 100 kHz to 10 mHz. EIS experiments were carried out under both dark and illumination conditions, in order to determine the electrocatalytic and photoelectrocatalytic properties of the samples. Illumination was provided by a 1000 W Xe light source at a wavelength of 360 nm. The capacitance of

the interface, necessary to perform Mott-Schottky analysis, was calculated under dark conditions at a constant frequency of 5 kHz using a 10 mV amplitude signal and scanning the potential from 0.7 V to 0.1 V at a rate of 50 mV s⁻¹.

The photocurrent density was measured in a quartz glass three-electrode photoelectrochemical cell with a volume of 14 mL, irradiating the samples perpendicularly at a wavelength of 360 nm in a 0.1 M H₂SO₄ solution and scanning the potential from 0 to 1 V at a scan rate of 2 mV s⁻¹. The distance between the light source and the sample was 5 cm (light power density of 40 mW cm⁻²).

2.4. Photoelectrocatalytic experiments

The PEC degradation of atrazine (20 mg L⁻¹) was performed in the same quartz cell, at a bias potential of 1 V and irradiating the sample with a 360 nm light (equivalent to 3.44 eV). Experiments were performed under constant magnetic stirring in an acidic electrolyte (0.1 M H₂SO₄). Prior to the irradiation, samples were immersed in the atrazine solution for 30 minutes at their open circuit potential to reach initial equilibrium conditions.

2.5. Analytical methods

Samples (3 mL) were withdrawn from the quartz cell at different irradiation times to measure their absorbance by means of a Unicam UV4 UV/Vis spectrophotometer with quartz cubes, in the range between 190-320 nm. After the measuring, the aliquots were always put back inside the reactor.

HPLC determinations were performed with a Jasco Model PU-2089 pump, equipped with a photodiode array detector MD-2018 Plus and a Kinetex XB-C18 column, 100 x 4.6 mm, with a 2.6 μm particle size and a pore size of 100 \AA . The degradation of atrazine and the evolution of its intermediates were followed by injection of the different samples (20 μL), using a mobile phase of water/methanol and a flow rate which varied during the 30 min of record: the initial composition of the mobile phase was 95% water/5% methanol, at 0.2 mL min^{-1} . The flow rate was increased to 0.5 mL min^{-1} within the interval 7-10 min, and the composition was modified to 40% water/60% methanol between minute 5 and minute 15. UV detection of atrazine and the different intermediates was carried out at 223 nm.

The mineralization extent of the atrazine solution was evaluated through the measurement of Total Organic Carbon (TOC) and ion chromatography. TOC measurements were performed with a Shimadzu TOC-L analyzer. The formation of NO_3^- resulting from the oxidation of nitrogen atoms present in the atrazine molecule was monitored by suppressed ion chromatography with a Metrohm 883 Basic IC plus ion chromatograph equipped with a Metrosep A Supp 5⁻ (150/4 mm) separation column. The eluent was a carbonate/bicarbonate (3.2/1 mM) buffer solution at a flow rate of 0.7 mL min^{-1} and the suppressor was a 0.1 M H_2SO_4 solution.

3. RESULTS AND DISCUSSION

3.1. Morphological characterization of the WO_3 nanostructure

Figure 1a – Figure 1c show the FESEM top images of the WO_3 nanostructure used in the present study. The structure consisted of very small nanosheets or nanowires, associated forming a kind of conical macrostructure. The cross section of the nanostructure is shown in **Figure 1d**. It can be observed that many layers containing these minuscule nanosheets or nanowires were formed. The thickness of this nanostructured layer has been determined to be $2.1 \pm 0.3 \mu\text{m}$. The very small size of these nanostructures has been related in a previous work to the presence of the bidentate ligands O_2^{2-} in the anodization electrolyte, which inhibited the growth of the nanostructures during the fabrication process [53]. This particular morphology and size resulted in very high electroactive surface areas, providing high photoelectrochemical efficiencies.

Raman spectra of the as-anodized and annealed WO_3 nanostructures are shown in **Figure 2a**. Several common peaks can be clearly discerned in both spectra: 191 cm^{-1} , 270 cm^{-1} , 644 cm^{-1} , 715 cm^{-1} and 815 cm^{-1} , although their intensity was much more marked for the annealed sample. These peaks are generally associated with the monoclinic crystalline form of WO_3 [54-57]. On the other hand, a small peak centered at $\sim 950 \text{ cm}^{-1}$ can also be observed in both spectra. This peak has been related to amorphous $\text{WO}_3 \cdot n(\text{H}_2\text{O})$ hydrated oxide [55, 57]. These results indicate, first, that the as-anodized nanostructures had a crystalline structure, at least partially, and second, that after annealing this crystalline structure was favored through a dehydration process. In order to confirm the composition of the annealed WO_3 nanostructure, an EDX spectrum is presented in **Figure 2b**. Peaks of tungsten and oxygen can clearly be seen, confirming that WO_3 was formed.

3.2. Electrochemical and photoelectrochemical characterization of the WO₃ nanostructure

The electrochemical properties of the WO₃ nanostructure were investigated by means of cyclic voltammetry (using a Ferro/Ferri redox couple), EIS under a potential polarization of 0.7 V and Mott-Schottky analysis. Cyclic voltammograms of the WO₃ nanostructure and of a WO₃ compact film are presented in **Figure 3**. It can be clearly seen that the voltammogram of the WO₃ nanostructure showed the typical electrochemical response of the Ferro/Ferri redox couple, with two peaks, one anodic at 0.46 V, and another cathodic at 0.29 V. On the other hand, the current signal of the WO₃ compact layer was almost flat. This behavior can be attributed to the greatly enhanced electrochemical activity of the WO₃ nanostructure due to an important increase of the electrode active area.

Figure 4 and **Figure 5** show the EIS results for the WO₃ nanostructure and for the WO₃ compact layer, in the form of Nyquist and Bode-phase diagrams, under dark and illumination conditions, respectively. For both samples, Nyquist plots exhibited two unfinished semicircles (under dark conditions, **Figure 4a**) and two almost-finished semicircles (under illumination, **Figure 5a**), while Bode-phase plots showed two peaks at intermediate and low frequencies. The first semicircle, associated with the phase angle peak recorded within the frequency interval between 10-100 Hz, has for both samples a noticeably lower amplitude than the second one (see inset in **Figures 4a** and **Figure 5a**), associated with the phase angle peak recorded at low frequencies (0.1-0.01 Hz). It can be observed from **Figure 4a** and **Figure 5a** that both semicircles were much larger for the WO₃ compact layer than for the nanostructure, indicating considerably

higher electrochemical resistances of the former. These resistances can be determined by fitting the experimental EIS results with an equivalent circuit. The circuit chosen in this work is shown in **Figure 6** (two RC time constant in parallel distributed hierarchically), where constant phase elements (CPEs) have been used instead of pure capacitors to account for frequency dispersion and non-ideal behaviors. In the equivalent circuit, R_S represents the electrolyte resistance for both cases. The time constant R_1/CPE_1 explains the behavior of the semiconductor (WO_3)/electrolyte interface (compact layer/electrolyte and nanostructure/electrolyte interfaces). The second time constant (R_2/CPE_2) for the compact layer explains the electrochemical properties of the oxide film, while for the WO_3 nanostructure, R_2/CPE_2 can be associated with the charge transfer processes at the bottom of the nanostructured WO_3 or with a compact WO_3 film beneath the nanostructure [58].

The values of R_S , R_1 and R_2 are shown in **Table 1** for both WO_3 samples under dark and illumination conditions. Under dark conditions, for the compact layer, R_1 and R_2 are of the order of tens and hundreds of $k\Omega$, respectively. For the nanostructure, R_2 is of the same order of magnitude to that obtained for the compact layer, but R_1 is significantly lower. Under illumination, resistance values are significantly lower than under dark conditions, regardless of the sample. This fact is related to the generation of charge carriers upon illumination of the electrodes, hence reducing charge transfer resistances. For the WO_3 nanostructure, R_1 and R_2 values are, again, much lower than for the compact WO_3 layer. These values mean that the WO_3 nanostructure has a much lower resistance to charge-transfer processes than the WO_3 compact layer, both under dark and illumination conditions, which can be explained by an increase in the number of electrochemically active sites due to a higher surface area exposed to the electrolyte.

Since R_I has been defined above as the charge transfer resistance at the semiconductor (WO_3)/electrolyte interface, this parameter will be used to quantitatively compare the electrochemical and photoelectrochemical behavior of both samples. Under dark conditions, interfacial charge transfer resistance (R_I) was 16 times higher for the compact WO_3 layer than for the WO_3 nanostructure. Under illumination conditions, R_I was more than 43 times higher for the compact WO_3 layer than for the WO_3 nanostructure. These results imply, first, that by nanostructuring the photoelectrode, the number of electrochemically active sites noticeably increased and, second, that there was a synergistic effect between increasing the surface area and illuminating the photoanode, since the increase in R_I was higher under illumination than under dark conditions. These results are also consistent with the much higher redox peaks observed in the voltammograms of **Figure 3**.

Mott-Schottky analysis was also performed to study the semiconducting properties of the WO_3 nanostructure. For n -type semiconductors, such as WO_3 , the capacitance of the semiconductor/electrolyte interface, C , can be described by the following Mott-Schottky relationship:

$$\frac{1}{C^2} = \frac{2}{\epsilon\epsilon_0 e N_D} \left(E - E_{FB} - \frac{kT}{e} \right) \quad (1)$$

where ϵ represents the dielectric constant of the semiconductor (a value of 50 has been assumed for WO_3 [59]), ϵ_0 is the vacuum permittivity ($8.85 \cdot 10^{-14}$ F cm⁻¹), e is the electron charge ($1.60 \cdot 10^{-19}$ C), N_D is the donor density, E_{FB} is the flat-band potential, k is the Boltzmann constant ($1.38 \cdot 10^{-23}$ J/K) and T is the absolute temperature.

Figure 7 shows the Mott-Schottky plot of the WO_3 nanostructure obtained at a constant frequency of 5 kHz and carried out under dark conditions not to modify the distribution of charge carriers within the semiconducting WO_3 nanostructure. The N_D and E_{FB} values were determined from the linear region slope of the C^{-2} vs. E representation and from the x-intercept (at $C^{-2} = 0$), respectively. The calculated values were $N_D = 9.2 \times 10^{19} \text{ cm}^{-3}$ and $E_{FB} = 0.203 \text{ V}$. The donor density (typically oxygen vacancies in the crystalline WO_3) is somewhat lower than other values reported earlier for WO_3 nanostructures [59-64], which can be beneficial, since oxygen vacancies can act as traps for photogenerated electrons, thus enhancing electron/hole recombination [65, 66].

On the other hand, at potential values more positive than the E_{FB} , which is the potential that has to be applied to the semiconductor to eliminate the band bending, a depletion layer allowing the separation of the photogenerated electrons and holes is formed within the semiconductor. Therefore, the E_{FB} is the onset potential for anodic photocurrents. Moreover, since N_D is of the order of 10^{19} - 10^{20} , the WO_3 nanostructure can be regarded as a heavily doped semiconductor. This implies that its Fermi level is placed right below the lower edge of the conduction band. Since the flat-band potential denotes the position of that Fermi level at the surface of a given semiconductor with respect to a reference electrode, the E_{FB} value can be used to give the position of the conduction band edge for a n -type semiconductor [67, 68]. Once the position of the conduction band is known, the position of the valence band can be easily placed using the band-gap of the semiconductor, taking into account that the relationship between the electron energy in the vacuum (which is the reference used in semiconductor solid-state physics to position the energy band edges) and a redox potential E_{redox} with respect to the normal hydrogen potential (NHE, used in electrochemistry) is [69, 70]:

$$E_{F,redox} = -4.44(\pm 0.02)\text{eV} - eE_{redox}(\text{eV}) \quad \text{at } 298.15 \text{ K} \quad (2)$$

where $E_{F,redox}$ is the Fermi level expressed with respect to the vacuum reference (in eV). Therefore, a value of $E_{FB} = 0.203 \text{ V}_{\text{Ag/AgCl (3M KCl)}} \equiv 0.408 \text{ V}_{\text{SHE}}$ can be written as -4.848 eV. Since the band gap for crystalline WO_3 nanostructures has been reported to be between 2.5-2.7 eV [51, 52, 64, 71], the valence band of the WO_3 nanostructure under study has an energy of -7.448 eV (assuming a band gap of 2.6 eV), which translated to the redox potential scale is $3.008 \text{ V}_{\text{NHE}} \equiv 2.803 \text{ V}_{\text{Ag/AgCl (3M KCl)}}$, a value very similar to others reported in the literature [72]. This highly positive potential is the potential of the photogenerated holes in the WO_3 valence band, which indicates the extreme oxidative power of these species in WO_3 nanostructures.

The photocurrent density-potential (i_{ph} - E) behavior of the WO_3 nanostructure under a constant illumination at 360 nm is presented in **Figure 8**. A curve under dark conditions is also shown. Without illumination, the sample exhibited very low current densities, especially at high polarization ($i = 4.8 \mu\text{A cm}^{-2}$ at $E = 1 \text{ V}$). However, under illumination, photocurrent density values started increasing at potentials more positive than the onset potential for photocurrent densities, $\sim 0.2 \text{ V}$, which coincides with the E_{FB} calculated above. At 1 V, the i_{ph} value was 0.88 mA cm^{-2} , almost 200 times higher than the corresponding dark current density.

3.3. Photoelectrodegradation of atrazine

3.3.1. UV absorbance

Figure 9 shows the temporal change in the UV absorption spectra of the 20 ppm atrazine solution in 0.1 M H₂SO₄ after irradiation at 360 nm with an external potential polarization of 1 V. It can be observed that the initial spectrum of atrazine has a maximum absorbance peak at 220 nm and a less intense peak centered at 277 nm. The 220 nm band has been assigned in the literature to the excitation of an electron from a π -bonding orbital to an antibonding π^* orbital (a π to π^* transition) [33, 36], while the band observed at 277 nm has been related to the promotion of a non-bonding electron from a lone-pair orbital of a nitrogen atom to a π -bonding orbital of the *s*-triazine ring [73].

The peak at 277 nm progressively decreased with irradiation time until its complete disappearance at ~ 150 min, while the high-absorbance peak at 220 nm decreased with time and underwent a gradual bathochromic shift or red-shift, which stopped at 233 nm (**Figure 9 (a)**). This red-shift can be associated with the incorporation of auxochrome groups (like -OH and/or -NH₂) in the ring, hence modifying the ability of the chromophore *s*-triazine ring to absorb light and increasing to some extent its absorption wavelength. Therefore, that shift can be explained by the formation of primary substitution products, like 2-hydroxy intermediates due to a dechlorination-hydroxylation mechanism (such as 2-hydroxyatrazine) and dealkylated derivatives due to 4,6-lateral chain oxidation (such as de-ethyl atrazine or de-isopropyl atrazine). These products have been reported as intermediates in the literature on the photocatalytic degradation of atrazine with TiO₂ [18, 32, 35, 38-43].

The disappearance of the peak at 233 nm upon prolonged photoelectrocatalysis (**Figure 9 (b)**) indicates further reaction of those intermediate species to form secondary by-products. The growth of absorbance values in the 200-215 nm at longer irradiation times (from 150 minutes on, see **Figure 9 (b)**), which eventually led to the formation of a new absorption band centered at 204 nm, can be related to the formation of these secondary intermediates, such as ammeline, ammelide or cyanuric acid [36].

3.3.2. HPLC analysis

HPLC chromatograms obtained during atrazine photoelectrocatalytic degradation at different times are shown in **Figure 10**. The initial chromatogram shows a single peak, at a retention time of $t_R = 22.3$ min, which corresponds to atrazine (peak A). This peak decreased with irradiation time until completely disappearing at $t > 180$ min. The degradation of atrazine resulted in the formation of intermediate species, since additional peaks could be observed in the chromatograms. After 30 min of irradiation, a peak at $t_R = 18.4$ min was clearly observed (peak B), which decreased gradually and was almost eliminated after 360 min of PEC reaction. After comparing the retention times and the UV absorption spectra, this peak has been identified as 2-hydroxyatrazine.

At retention times between 4-6 min, other peaks evolved, indicating the formation, accumulation and degradation of further intermediate products. Finally, after 1320 min of irradiation, an intense single peak could still be observed between 4.7-4.8 min (the much smaller peak at $t_R = 12$ min can be associated with the elution of the solvent front upon changing its composition and flow rate, as explained in the experimental procedure). All these peaks, seen at relatively short retention times, could be related to

the formation of hydroxylated and dealkylated derivatives, such as ammeline, ammelide and cyanuric acid. The retention times of these compounds were all located within the range 4-5.5 min, but their accurate identification was not possible, probably due to co-elution between them.

Figure 11a illustrates the atrazine photoelectrodegradation over time. It can be seen that the degradation process was very fast within the first 30 minutes, and after that it somewhat slowed down. Degradation efficiencies reached values close to 100 % after 180 min of irradiation.

The previous results can be approximated to pseudo-first order kinetics to estimate the apparent kinetic coefficient, k_{app} , which can be extracted from the slope of the linear representation $\ln(C/C_0)$ vs. t (**Figure 11b**). In this case, $k_{app} = 0.0233 \text{ min}^{-1}$ or 1.398 h^{-1} , which is higher than most kinetics coefficients found in the literature for the photodegradation and photoelectrodegradation of atrazine [32, 34, 42-45, 50].

Moreover, if some factors such as the amount of photocatalyst used are taken into account, the good behavior of WO_3 photoanodes developed in this work is still more remarkable. For example, in the works referenced above, photocatalyst concentrations between 500-1500 mg/l were used. In the present study, assuming that the nanostructured WO_3 layer is a compact cylinder, the mass of WO_3 used in the present work can be calculated as 0.756 mg. Dividing that value by the volume of atrazine solution used (14 ml), the photocatalyst concentration is $\sim 54 \text{ mg/L}$. Notice that this value is a maximum value, since the nanostructured layer has been assimilated to a compact one in order to calculate the volume of the cylinder, so the real photocatalyst

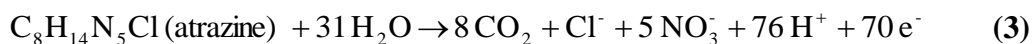
mass would be significantly lower than the 0.756 mg written above. These results demonstrate that in spite of using an amount of photocatalyst 10-30 times lower than in other studies, the kinetic coefficient was higher in this work.

Another factor that needs to be contemplated when comparing kinetic coefficients in PEC is the exposed area of the photoanode and the ratio between this area and the solution volume. In the present work, both the photoanode area (0.5 cm^2) and the ratio between this area and the volume solution ($35.7 \text{ cm}^2 \text{ L}^{-1}$) were lower than in other studies dealing with the PEC degradation of atrazine with TiO_2 -based photoanodes [18].

In view of these explanations, it can be said that WO_3 nanosheets employed in this work are efficient for their use as photoanodes in PEC degradation of atrazine.

3.3.3. Extent of mineralization: TOC and Ion chromatography

The overall process of atrazine mineralization can be described by the following reaction [28, 30]:



The TOC of the initial atrazine solution (20 ppm) was determined as 8.951 ppm (very similar to the theoretical value of 8.902 ppm). After 22 h of PEC degradation (1320 min), the measured TOC was 2.518 ppm. This means that 2.26 out of 8 carbon atoms remained in the solution, i.e., the five carbon atoms of the lateral chains were completely mineralized and the triazine ring was partially broken.

On the other hand, the NO_3^- evolution with reaction time can provide further information on the extent of the atrazine mineralization reaction. **Figure 12** shows the time evolution of the NO_3^- moles/initial atrazine moles ratio, measured by ion chromatography. It can be observed that NO_3^- concentration increased with irradiation time, at first slowly, but after 90 min of reaction, it began to increase faster, until reaching an approximately constant ratio value of ~ 2.5 at 240 min. At longer reaction times (1320 min, not shown in this figure), the molar ratio was about 3. These results imply that a total atrazine mineralization was not achieved (the molar ratio should be 5), as was deduced from the peaks which were still present in the UV absorption spectra and in the HPLC chromatograms at long reaction times. However, values of that ratio higher than 2 indicate that, apart from the oxidation of the two nitrogen atoms of the lateral-chain amino groups, the *s*-triazine ring in cyanuric acid, which is widely regarded as the final intermediate in the degradation of atrazine, was also broken to some extent due to the carbon-amino bond cleavage. This result is consistent with the TOC measured after 1320 min of PEC degradation.

3.3.4. Degradation mechanism

In general, two routes have been described in the literature for the atrazine degradation mechanism: (1) dechlorination-hydroxylation followed by dealkylation and subsequent deamination, and (2) dealkylation as the first step and then deamination and/or dechlorination-hydroxylation. In many studies dealing with the photolytic degradation of atrazine, the first route has been frequently reported, with 2-hydroxyatrazine and hydroxylated compounds as main intermediate products [32, 33, 35, 36, 41], while in

photocatalytic processes using TiO_2 , the main degradation route is normally the second one, i.e., the dealkylation by 4,6-lateral chain oxidation [32, 35, 38, 39, 41, 42, 46]. In the present study, and according to the HPLC results presented above (**Figure 10**), it seems clear that the main intermediate product of PCE atrazine degradation using a WO_3 nanostructure was 2-hydroxyatrazine, so the main degradation route for atrazine involved first the dechlorination-hydroxylation of the molecule, followed by the oxidation of the lateral chains to form dealkylated species, and the substitution of the amino groups by hydroxyl molecules, resulting in ammeline and cyanuric acid. On that basis, a simplified scheme showing the reaction sequence from atrazine to cyanuric acid is shown in **Figure 13**. The same conclusion has been reached by other authors using photoelectrocatalytic processes to remove atrazine from aqueous solutions [18]. Finally, and in line with the TOC and ion chromatography results, the *s*-triazine ring in cyanuric acid seemed to be partially open and further oxidized. It is important to remark that, in spite of the small amount of photoelectrocatalyst used, cyanuric acid was partially degraded. Cyanuric acid degradation has been reported before in the literature by using anodic oxidation and electro-Fenton with a BDD anode [27, 29]. However, partial degradation results presented in this work represent an important advance in PC and PEC mineralization of atrazine.

4. CONCLUSIONS

A high electroactive WO_3 nanostructure was synthesized by anodization in acidic media and in the presence of a small amount (0.05 M) of H_2O_2 , as it was demonstrated by cyclic voltammetric measurements using the $\text{Fe}(\text{CN})_6^{4-/3-}$ system. Moreover, the

resistance of this nanostructure to charge-transfer processes was much lower than that of a WO₃ compact layer.

From Mott-Schottky analysis, the flat-band potential of the WO₃ nanostructure was determined and, from that value, the position of its conduction and valence bands. The redox potential of photogenerated holes was calculated to be 3.008 V_{NHE}, indicating the extremely oxidant properties of these species in WO₃ nanostructures.

Atrazine was completely eliminated after ~180 min of PEC reaction following pseudo-first order kinetics, and intermediate species evolved subsequently with reaction time. The major intermediate species formed during the PEC degradation of atrazine using a WO₃ nanostructure was found to be 2-hydroxyatrazine. Hence, the main degradation pathway was dechlorination-hydroxylation followed by dealkylation.

The PEC method using a nanostructured WO₃ photoanode is capable of partially breaking down the atrazine molecule, possibly rupturing the heterocyclic ring, a step that is often considered as difficult.

Acknowledgements

Authors thank for the financial support to the Ministerio de Economía y Competitividad (Project Code: CTQ2016-79203-R) and for the co-finance by the European Social Fund and to Dr. Carlos Carbonell Alcaina for the use of the HPLC and for providing technical support.

5. REFERENCES

- [1] Water quality and health strategy 2013-2020. World Health Organization, 2013.
- [2] The Millennium Development Goals Report 2015. Statistics Division of the United Nations Department of Economic and Social Affairs, 2015.
- [3] E. D. Ongley. Pesticides as water pollutants, in Control of water pollution from agriculture - FAO irrigation and drainage paper 55 (Food and Agriculture Organization of the United Nations, FAO), Rome, 1996, (Chapter 4).
- [4] E. D. Ongley. Introduction to agricultural water pollution, in Control of water pollution from agriculture - FAO irrigation and drainage paper 55 (Food and Agriculture Organization of the United Nations, FAO), Rome, 1996, (Chapter 1).
- [5] K. Parris, Impact of Agriculture on Water Pollution in OECD Countries: Recent Trends and Future Prospects, *Int. J. Water Resour. D.* 27 (2011) 33-52.
- [6] S. R. Müller, M. Berg, M. M. Ulrich, R. P. Schwarzenbach, Atrazine and Its Primary Metabolites in Swiss Lakes: Input Characteristics and Long-Term Behavior in the Water Column, *Environ. Sci. Technol.* 31 (1997) 2104-2113.
- [7] D. A. Goolsby, E. M. Thurman, M. L. Pomes, M. T. Meyer, W. A. Battaglin, Herbicides and Their Metabolites in Rainfall: Origin, Transport, and Deposition Patterns across the Midwestern and Northeastern United States, 1990-1991, *Environ. Sci. Technol.* 31 (1997) 1325-1333.
- [8] S. M. Miller, C. W. Sweet, J. V. DePinto, K. C. Hornbuckle, Atrazine and Nutrients in Precipitation: Results from the Lake Michigan Mass Balance Study, *Environ. Sci. Technol.* 34 (2000) 55-61.
- [9] M. Graymore, F. Stagnitti, G. Allinson, Impacts of atrazine in aquatic ecosystems, *Environ. Int.* 26 (2001) 483-495.
- [10] M. Neumann, R. Schulz, K. Schäfer, W. Müller, W. Mannheller, M. Liess, The significance of entry routes as point and non-point sources of pesticides in small streams, *Water Res.* 36 (2002) 835-842.
- [11] A. Hildebrandt, M. Guillamón, S. Lacorte, R. Tauler, D. Barceló, Impact of pesticides used in agriculture and vineyards to surface and groundwater quality (North Spain), *Water Res.* 42 (2008) 3315-3326.
- [12] Atrazine Information - European Chemicals Agency (ECHA) (<https://echa.europa.eu/substance-information/-/substanceinfo/100.016.017>) (accessed 2 November 2017).
- [13] X. Dong, L. Zhu, J. Wang, J. Wang, H. Xie, X. Hou, W. Jia, Effects of atrazine on cytochrome P450 enzymes of zebrafish (*Danio rerio*), *Chemosphere* 77 (2009) 404-412.

- [14] Y. L. Phyu, M. S. Warne, R. P. Lim, Toxicity and bioavailability of atrazine and molinate to the freshwater shrimp (*Paratya australiensis*) under laboratory and simulated field conditions, *Ecotox. Environ. Safe.* 60 (2005) 113-122.
- [15] T. B. Hayes, V. Khoury, A. Narayan, M. Nazir, A. Park, T. Brown, L. Adame, E. Chan, D. Buchholz, T. Stueve, S. Gallipeau, Atrazine induces complete feminization and chemical castration in male African clawed frogs (*Xenopus laevis*), *P. Natl. Acad. Sci. USA* 107 (2010) 4612-4617.
- [16] Public Health Statement: Atrazine - Agency for Toxic Substances and Disease Registry (ATSDR) (<https://www.atsdr.cdc.gov/phs/phs.asp?id=336&tid=59>) (accessed 2 November 2017).
- [17] W. Fan, T. Yanase, H. Morinaga, S. Gondo, T. Okabe, M. Nomura, T. Komatsu, K. Morohashi, T. B. Hayes, R. Takayanagi, H. Nawata, Atrazine-induced aromatase expression is SF-1 dependent: implications for endocrine disruption in wildlife and reproductive cancers in humans, *Environ. Health Perspect.* 115 (2007) 720-727.
- [18] S. Komtchou, A. Dirany, P. Drogui, N. Delegan, M. A. El Khakani, D. Robert, P. Lafrance, Degradation of atrazine in aqueous solution with electrophotocatalytic process using TiO_{2-x} photoanode, *Chemosphere* 157 (2016) 79-88.
- [19] 2004/248/EC: European Commission Decision of 10 March 2004 (<http://eur-lex.europa.eu/legal-content/EN/TXT/?uri=CELEX%3A32004D0248>).
- [20] Atrazine - Background and Updates - United States Environmental Protection Agency (EPA) (<https://www.epa.gov/ingredients-used-pesticide-products/atrazine-background-and-updates>). (accessed 2 November 2017).
- [21] H. Jiang, C. Adams, Treatability of chloro-s-triazines by conventional drinking water treatment technologies, *Water Res.* 40 (2006) 1657-1667.
- [22] M. A. Gondal, M. A. Suliman, M. A. Dastageer, G. K. Chuah, C. Basheer, D. Yang, A. Suwaiyan, Visible light photocatalytic degradation of herbicide (Atrazine) using surface plasmon resonance induced in mesoporous $\text{Ag-WO}_3/\text{SBA-15}$ composite, *J. Mol. Catal. A: Chem.* 425 (2016) 208-216.
- [23] M. A. Rodrigo, N. Oturan, M. A. Oturan, Electrochemically Assisted Remediation of Pesticides in Soils and Water: A Review, *Chem. Rev.* 114 (2014) 8720-8745.
- [24] M. J. Farré, M. I. Franch, S. Malato, J. A. Ayllón, J. Peral, X. Doménech, Degradation of some biorecalcitrant pesticides by homogeneous and heterogeneous photocatalytic ozonation, *Chemosphere* 58 (2005) 1127-1133.
- [25] K. H. Chan, W. Chu, Model Applications and Intermediates Quantification of Atrazine Degradation by UV-Enhanced Fenton Process, *J. Agric. Food Chem.* 54 (2006) 1804-1813.

- [26] M. H. Pérez, G. Peñuela, M. I. Maldonado, O. Malato, P. Fernández-Ibáñez, I. Oller, W. Gernjak, S. Malato, Degradation of pesticides in water using solar advanced oxidation processes, *Appl. Catal. B: Environ.* 64 (2006) 272-281.
- [27] B. Balci, N. Oturan, R. Cherrier, M. A. Oturan, Degradation of atrazine in aqueous medium by electrocatalytically generated hydroxyl radicals. A kinetic and mechanistic study, *Water Res.* 43 (2009) 1924-1934.
- [28] N. Borrás, R. Oliver, C. Arias, E. Brillas, Degradation of Atrazine by Electrochemical Advanced Oxidation Processes Using a Boron-Doped Diamond Anode, *J. Phys. Chem. A* 114 (2010) 6613-6621.
- [29] N. Oturan, E. Brillas, M. A. Oturan, Unprecedented total mineralization of atrazine and cyanuric acid by anodic oxidation and electro-Fenton with a boron-doped diamond anode, *Environ. Chem. Lett.* 10 (2012) 165-170.
- [30] B. R. Garza-Campos, J. L. Guzmán-Mar, L. H. Reyes, E. Brillas, A. Hernández-Ramírez, E. J. Ruiz-Ruiz, Coupling of solar photoelectro-Fenton with a BDD anode and solar heterogeneous photocatalysis for the mineralization of the herbicide atrazine, *Chemosphere* 97 (2014) 26-33.
- [31] S. Horikoshi, Y. Wada, N. Watanabe, H. Hidaka, N. Serpone, Near-quantitative mineralization of two refractory triazines under hydrothermal-supercritical aqueous conditions assisted by ozone and UV/ozone, *New J. Chem.* 27 (2003) 1216-1223.
- [32] V. Héquet, C. Gonzalez, P. Le Cloirec, Photochemical processes for atrazine degradation: methodological approach, *Water Res.* 35 (2001) 4253-4260.
- [33] M. E. D. G. Azenha, H. D. Burrows, L. Canle, R. Coimbra, M. I. Fernández, M. V. García, M. A. Peiteado, J. A. Santaballa, Kinetic and mechanistic aspects of the direct photodegradation of atrazine, atraton, ametryn and 2-hydroxyatrazine by 254nm light in aqueous solution, *J. Phys. Org. Chem.* 16 (2003) 498-503.
- [34] G. R. P. Malpass, D. W. Miwa, A. C. P. Miwa, S. A. S. Machado, A. J. Motheo, Photo-Assisted Electrochemical Oxidation of Atrazine on a Commercial Ti/Ru_{0.3}Ti_{0.7}O₂ DSA Electrode, *Environ. Sci. Technol.* 41 (2007) 7120-7125.
- [35] S. Jain, R. Yamgar, R. V. Jayaram, Photolytic and photocatalytic degradation of atrazine in the presence of activated carbon, *Chem. Eng. J.* 148 (2009) 342-347.
- [36] C. Chen, S. Yang, Y. Guo, C. Sun, C. Gu, B. Xu, Photolytic destruction of endocrine disruptor atrazine in aqueous solution under UV irradiation: Products and pathways, *J. Hazard. Mater.* 172 (2009) 675-684.
- [37] G. R. P. Malpass, D. W. Miwa, S. A. S. Machado, P. Olivi, A. J. Motheo, Oxidation of the pesticide atrazine at DSA electrodes, *J. Hazard. Mater.* 137 (2006) 565-572.

- [38] E. Pelizzetti, V. Maurino, C. Minero, V. Carlin, M. L. Tosato, E. Pramauro, O. Zerbini, Photocatalytic degradation of atrazine and other s-triazine herbicides, *Environ. Sci. Technol.* 24 (1990) 1559-1565.
- [39] E. Pelizzetti, C. Minero, E. Borgarello, L. Tinucci, N. Serpone, Photocatalytic activity and selectivity of titania colloids and particles prepared by the sol-gel technique: photooxidation of phenol and atrazine, *Langmuir* 9 (1993) 2995-3001.
- [40] C. Y. Chan, S. Tao, R. Dawson, P. K. Wong, Treatment of atrazine by integrating photocatalytic and biological processes, *Environ. Pollut.* 131 (2004) 45-54.
- [41] C. L. Bianchi, C. Pirola, V. Ragaini, E. Selli, Mechanism and efficiency of atrazine degradation under combined oxidation processes, *Appl. Catal. B: Environ.* 64 (2006) 131-138.
- [42] T. A. McMurray, P. S. M. Dunlop, J. A. Byrne, The photocatalytic degradation of atrazine on nanoparticulate TiO₂ films, *J. Photoch. Photobio. A* 182 (2006) 43-51.
- [43] J. Andersen, M. Pelaez, L. Guay, Z. Zhang, K. O'Shea, D. D. Dionysiou, NF-TiO₂ photocatalysis of amitrole and atrazine with addition of oxidants under simulated solar light: Emerging synergies, degradation intermediates, and reusable attributes, *J. Hazard. Mater.* 260 (2013) 569-575.
- [44] Y. Zhang, H. Wu, P. Liu, Enhanced Transformation of Atrazine by High Efficient Visible Light-Driven N, S-Codoped TiO₂ Nanowires Photocatalysts, *Int.J.Photoenergy* 2014 (2014) 1-8.
- [45] M. L. Yola, T. Eren, N. Atar, A novel efficient photocatalyst based on TiO₂ nanoparticles involved boron enrichment waste for photocatalytic degradation of atrazine, *Chem. Eng. J.* 250 (2014) 288-294.
- [46] W. K. Wang, J. J. Chen, M. Gao, Y. X. Huang, X. Zhang, H. Q. Yu, Photocatalytic degradation of atrazine by boron-doped TiO₂ with a tunable rutile/anatase ratio, *Appl. Catal. B: Environ.* 195 (2016) 69-76.
- [47] J. Romão, G. Mul, Substrate Specificity in Photocatalytic Degradation of Mixtures of Organic Contaminants in Water, *ACS Catal.* 6 (2016) 1254-1262.
- [48] R. Dagher, P. Drogui, D. Robert, Photoelectrocatalytic technologies for environmental applications, *J. Photoch. Photobio. A* 238 (2012) 41-52.
- [49] S. Garcia-Segura, E. Brillas, Applied photoelectrocatalysis on the degradation of organic pollutants in wastewaters, *J. Photoch. Photobio. C* 31 (2017) 1-35.
- [50] N. Lu, H. Zhao, J. Li, X. Quan, S. Chen, Characterization of boron-doped TiO₂ nanotube arrays prepared by electrochemical method and its visible light activity, *Sep. Purif. Technol.* 62 (2008) 668-673.

- [51] H. Zheng, J. Z. Ou, M. S. Strano, R. B. Kaner, A. Mitchell, K. Kalantar-zadeh, Nanostructured Tungsten Oxide - Properties, Synthesis, and Applications, *Adv. Funct. Mater.* 21 (2011) 2175-2196.
- [52] C. A. Bignozzi, S. Caramori, V. Cristino, R. Argazzi, L. Meda, A. Tacca, Nanostructured photoelectrodes based on WO₃: applications to photooxidation of aqueous electrolytes, *Chem. Soc. Rev.* 42 (2013) 2228-2246.
- [53] R. M. Fernández-Domene, R. Sánchez-Tovar, B. Lucas-Granados, G. Roselló-Márquez, J. García-Antón, A simple method to fabricate high-performance nanostructured WO₃ photocatalysts with adjusted morphology in the presence of complexing agents, *Mater. Design* 116 (2017) 160-170.
- [54] R. Sánchez-Tovar, R. M. Fernández-Domene, D. M. García-García, J. García-Antón, Enhancement of photoelectrochemical activity for water splitting by controlling hydrodynamic conditions on titanium anodization, *J. Power Sources* 286 (2015) 224-231.
- [55] C. Bittencourt, R. Landers, E. Llobet, X. Correig, J. Calderer. The role of oxygen partial pressure and annealing temperature on the formation of W=O bonds in thin WO₃ films, *Semicond. Sci. Technol.* 17 (2002) 522-525.
- [56] C. Santato, M. Odziemkowski, M. Ulmann, J. Augustynski. Crystallographically Oriented Mesoporous WO₃ Films: Synthesis, Characterization, and Applications, *J. Am. Chem. Soc.* 123 (2001) 10639-10649.
- [57] M. F. Daniel, B. Desbat, J. C. Lassegues, B. Gerand, M. Figlarz. Infrared and Raman study of WO₃ tungsten trioxides and WO₃·xH₂O tungsten trioxide hydrates, *J. Solid State Chem.* 67 (1987) 235-247.
- [58] R. M. Fernández-Domene, R. Sánchez-Tovar, E. Segura-Sanchís, J. García-Antón. Novel Tree-Like WO₃ Nanoplatelets with Very High Surface Area Synthesized by Anodization Under Controlled Hydrodynamic Conditions, *Chem. Eng. J.* 286 (2015) 59-67.
- [59] M. Yagi, S. Maruyama, K. Sone, K. Nagai, T. Norimatsu, Preparation and photoelectrocatalytic activity of a nano-structured WO₃ platelet film, *J. Solid State Chem.* 181 (2008) 175-182.
- [60] W. Li, J. Li, X. Wang, J. Ma, Q. Chen, Photoelectrochemical and physical properties of WO₃ films obtained by the polymeric precursor method, *Int. J. Hydrogen Energ.* 35 (2010) 13137-13145.
- [61] F. Amano, M. Tian, B. Ohtani, A. Chen, Photoelectrochemical properties of tungsten trioxide thin film electrodes prepared from facet-controlled rectangular platelets, *J. Solid State Electrochem.* 16 (2012) 1965-1973.
- [62] Y. Liu, Y. Li, W. Li, S. Han, C. Liu, Photoelectrochemical properties and photocatalytic activity of nitrogen-doped nanoporous WO₃ photoelectrodes under visible light, *Appl. Surf. Sci.* 258 (2012) 5038-5045.

- [63] G. Wang, Y. Ling, H. Wang, X. Yang, C. Wang, J. Z. Zhang, Y. Li, Hydrogen-treated WO₃ nanoflakes show enhanced photostability, *Energy Environ. Sci.* 5 (2012) 6180-6187.
- [64] R. M. Fernández-Domene, R. Sánchez-Tovar, B. Lucas-Granados, J. García-Antón, Improvement in photocatalytic activity of stable WO₃ nanoplatelet globular clusters arranged in a tree-like fashion: Influence of rotation velocity during anodization, *Appl. Catal. B Environ.* 189 (2016) 266-282.
- [65] H. Irie, Y. Watanabe, K. Hashimoto, Nitrogen-Concentration Dependence on Photocatalytic Activity of TiO_{2-x}N_x Powders, *J. Phys. Chem. B* 107 (2003) 5483-5486.
- [66] D. Wang, X. Zhang, P. Sun, S. Lu, L. Wang, C. Wang, Y. Liu, Photoelectrochemical Water Splitting with Rutile TiO₂ Nanowires Array: Synergistic Effect of Hydrogen Treatment and Surface Modification with Anatase Nanoparticles, *Electrochim. Acta* 130 (2014) 290-295.
- [67] R. van de Krol, Principles of Photoelectrochemical Cells, in: R. van de Krol, M. Grätzel (eds.), *Photoelectrochemical Hydrogen Production*. Springer, New York, 2012, pp. 13-67.
- [68] R. Beranek, (Photo)electrochemical Methods for the Determination of the Band Edge Positions of TiO₂-Based Nanomaterials, *Adv. Phys. Chem.* 2011 (2011) 1-20.
- [69] A. D. McNaught and A. Wilkinson, *IUPAC Compendium of Chemical Terminology - the Gold Book*, Blackwell Science, Oxford, 1997.
- [70] K. Rajeshwar, Fundamentals of Semiconductor Electrochemistry and Photoelectrochemistry, in: A. J. Bard, M. Stratmann, S. Licht (eds.), *Semiconductor Electrodes and Photoelectrochemistry (Encyclopedia of Electrochemistry, Volume 6)*, Weinheim, 2002, pp. 1-51.
- [71] W. Li, P. Da, Y. Zhang, Y. Wang, X. Lin, X. Gong, G. Zheng, WO₃ Nanoflakes for Enhanced Photoelectrochemical Conversion, *ACS Nano* 8 (2014) 11770-11777.
- [72] L. Weinhardt, M. Blum, M. Bär, C. Heske, B. Cole, B. Marsen, E. L. Miller, Electronic Surface Level Positions of WO₃ Thin Films for Photoelectrochemical Hydrogen Production, *J. Phys. Chem. C* 112 (2008) 3078-3082.
- [73] S. F. Mason, The electronic spectra of N-heteroaromatic systems. Part I. The n- π transitions of monocyclic azines, *J. Chem. Soc.* (1959) 1240-1246.

Table caption

Table 1. Resistance values obtained from fitting the EIS experimental results with the circuit shown in **Figure 6**.

Figures captions

Figure 1. FESEM images of the WO_3 nanostructure used in this study: (a) at 1000X, (b) at 5000X, (c) at 15000X, (d) cross section (15000X).

Figure 2. Raman spectra of the as-anodized and annealed WO_3 nanostructure (a); EDX spectrum of the annealed sample (b).

Figure 3. Cyclic voltammetry characterization of the WO_3 nanostructure and of a WO_3 compact layer in 10 mM $\text{Fe}(\text{CN})_6\text{K}_4$ + 0.1 M H_2SO_4 .

Figure 4. EIS results of the WO_3 nanostructure and of a WO_3 compact layer under dark conditions in 0.1 M H_2SO_4 , in the form of (a) Nyquist plots, and (b) Bode-phase plots.

Figure 5. EIS results of the WO_3 nanostructure and of a WO_3 compact layer under irradiation conditions in 0.1 M H_2SO_4 , in the form of (a) Nyquist plots, and (b) Bode-phase plots.

Figure 6. Equivalent circuit used to analyze the EIS results.

Figure 7. Mott-Schottky plot of the WO₃ nanostructure.

Figure 8. Dark current and photocurrent densities of the WO₃ nanostructure as a function of the applied potential.

Figure 9. UV absorption spectra obtained during PEC degradation of 20 ppm of atrazine at different reaction times: (a) from 0-150 min, (b) from 210-1320 min.

Figure 10. HPLC chromatograms of atrazine and its intermediates recorded at different reaction times. Peaks of atrazine (A) and 2-hydroxyatrazine (B) have been identified in the plots.

Figure 11. (a) Degradation profiles and efficiencies, and (b) pseudo-first order kinetics for the PEC degradation of 20 ppm of atrazine.

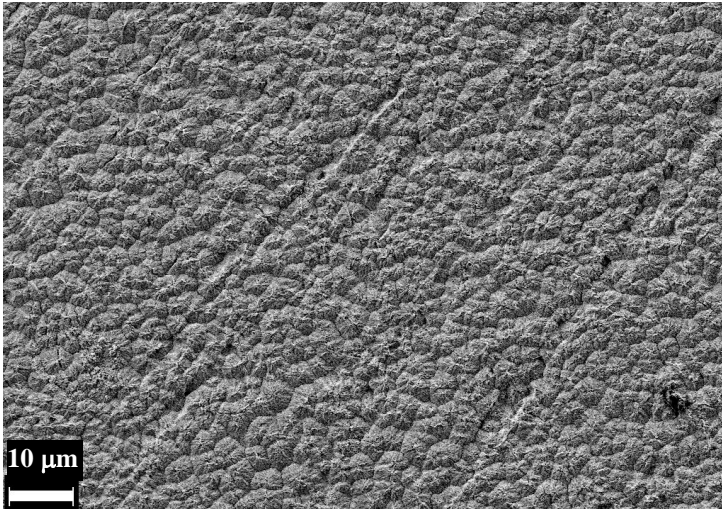
Figure 12. Time evolution of the NO₃⁻ moles/initial atrazine moles ratio during PEC degradation of 20 ppm of atrazine.

Figure 13. Schematic representation of the proposed PEC degradation mechanism for atrazine using a WO₃ nanostructure.

Table 1

	<i>WO₃ sample</i>	<i>R_S/Ω cm²</i>	<i>R₁/kΩ cm²</i>	<i>R₂/kΩ cm²</i>
Dark conditions	Compact layer	4.3 ± 0.4	46.3 ± 4.9	523 ± 36
	Nanostructure	6.4 ± 0.7	2.9 ± 0.3	184 ± 24
Illumination conditions	Compact layer	3.2 ± 0.2	2.6 ± 0.4	5.5 ± 0.9
	Nanostructure	5.9 ± 0.6	0.06 ± 0.01	1.7 ± 0.3

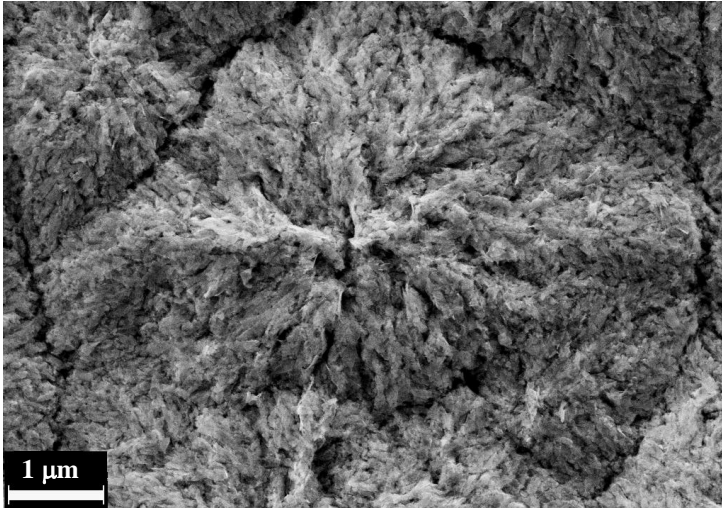
Figure 1



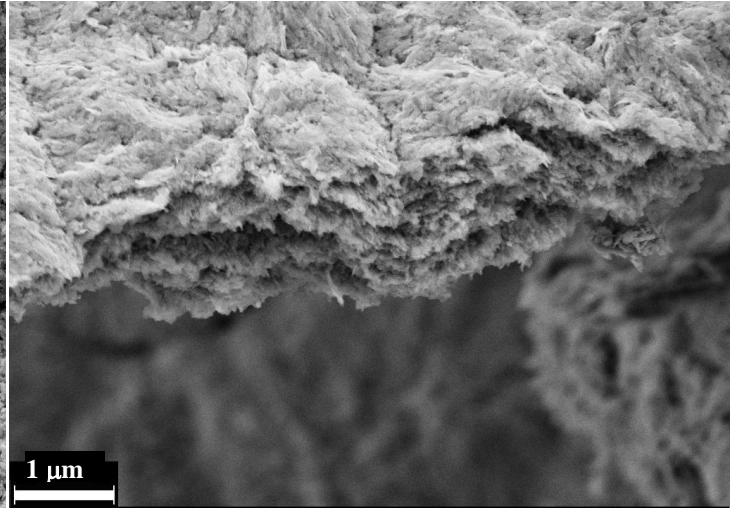
(a)



(b)

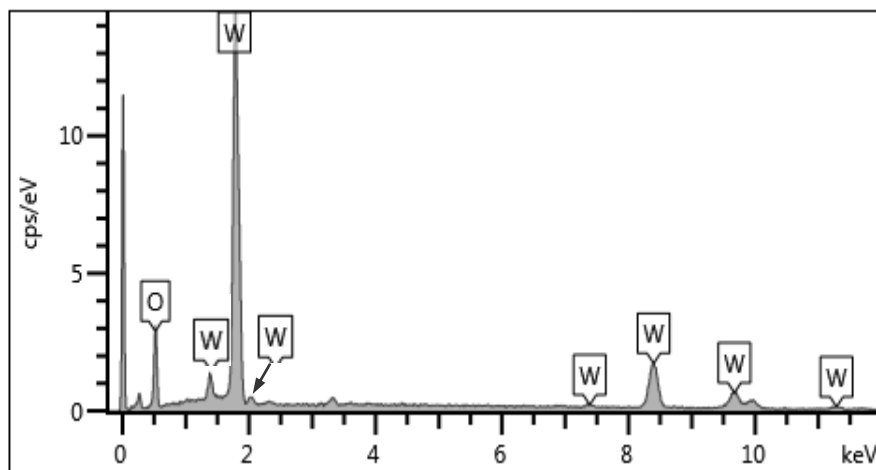
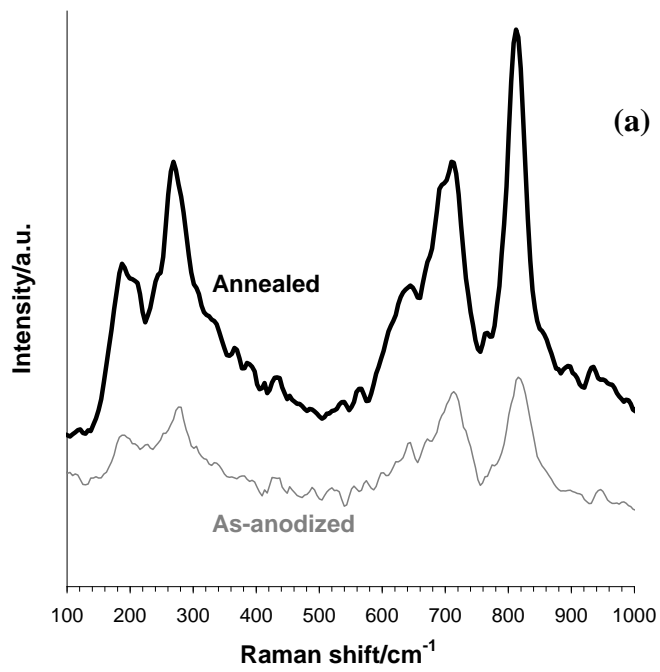


(c)



(d)

Figure 2



(b)

Figure 3

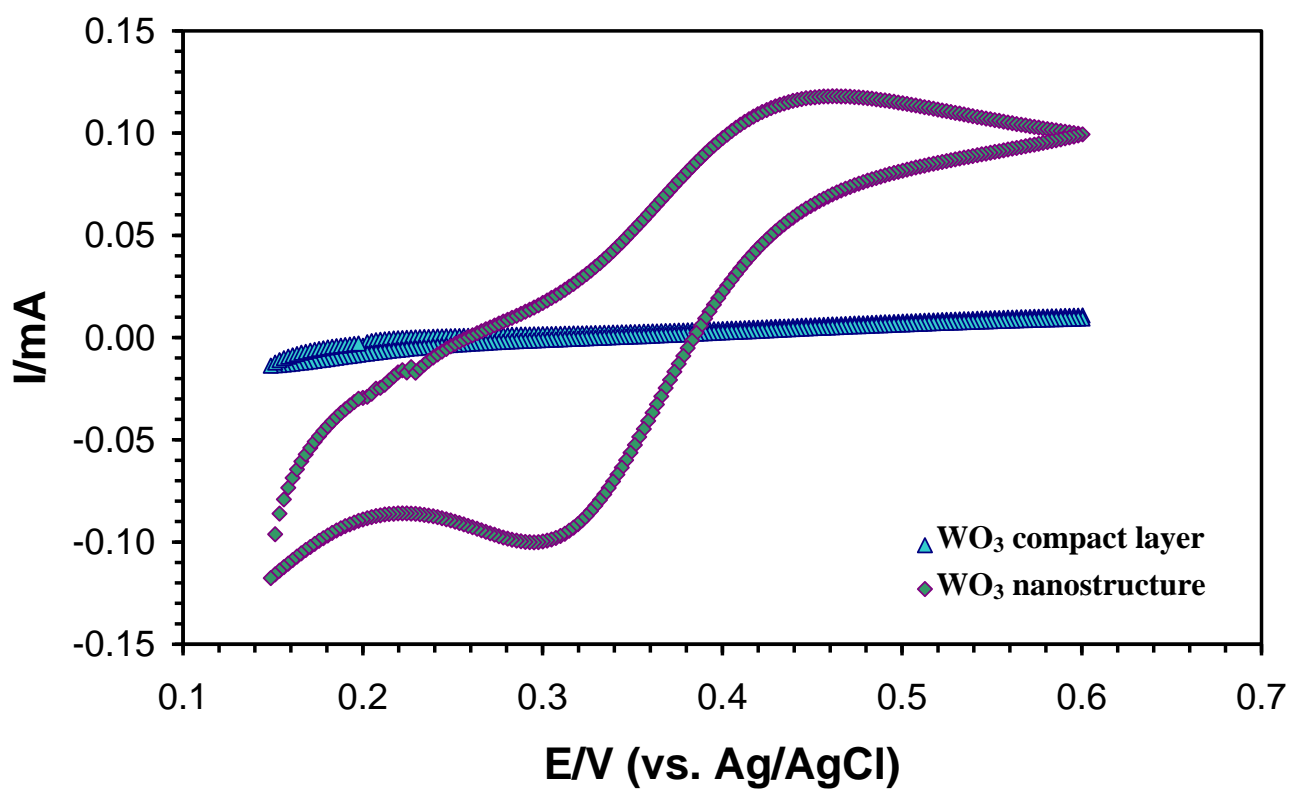


Figure 4

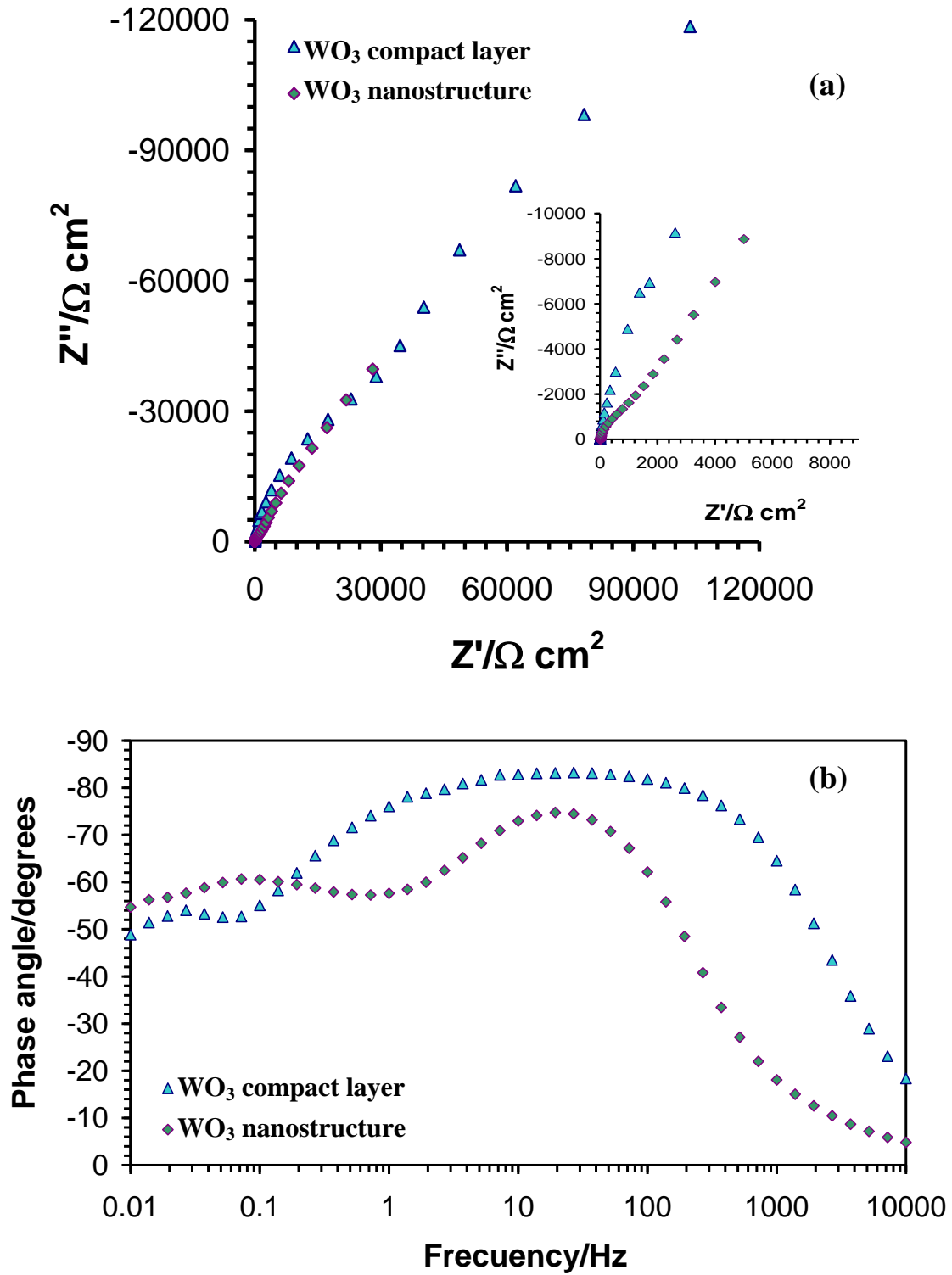


Figure 5

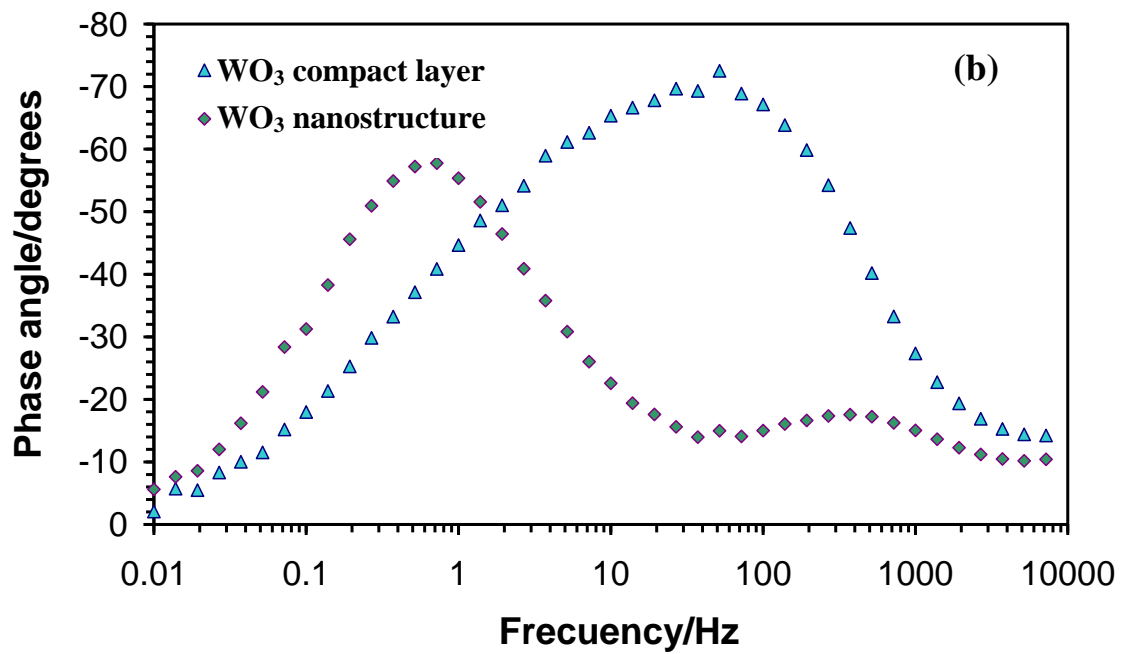
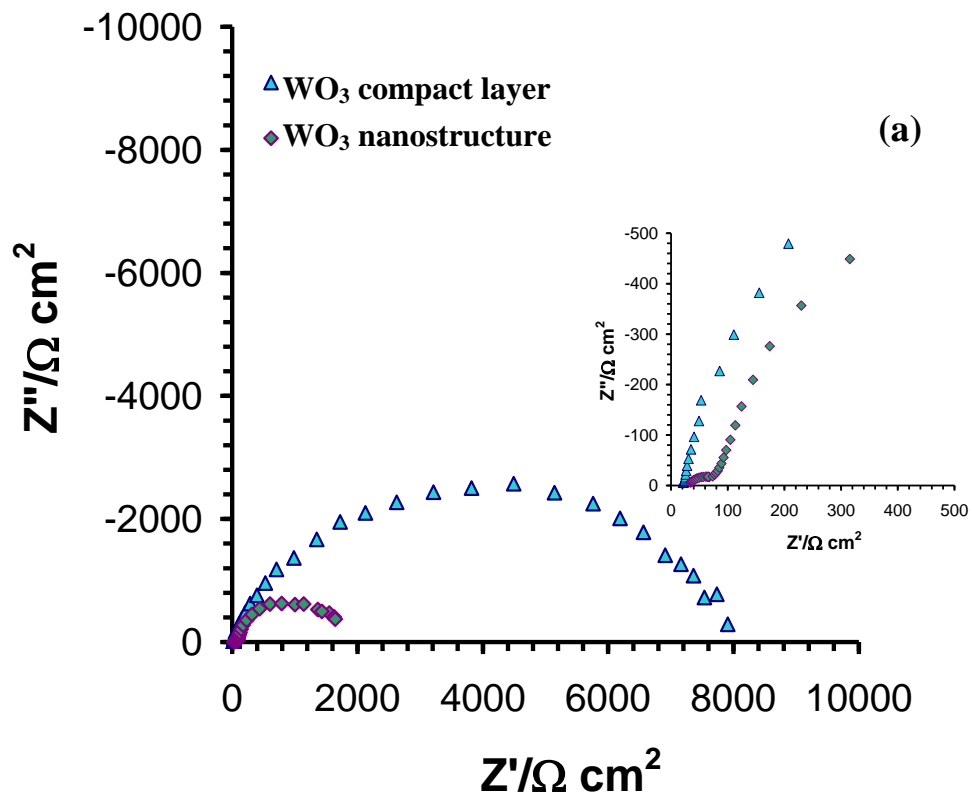


Figure 6

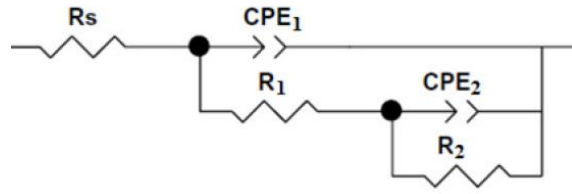


Figure 7

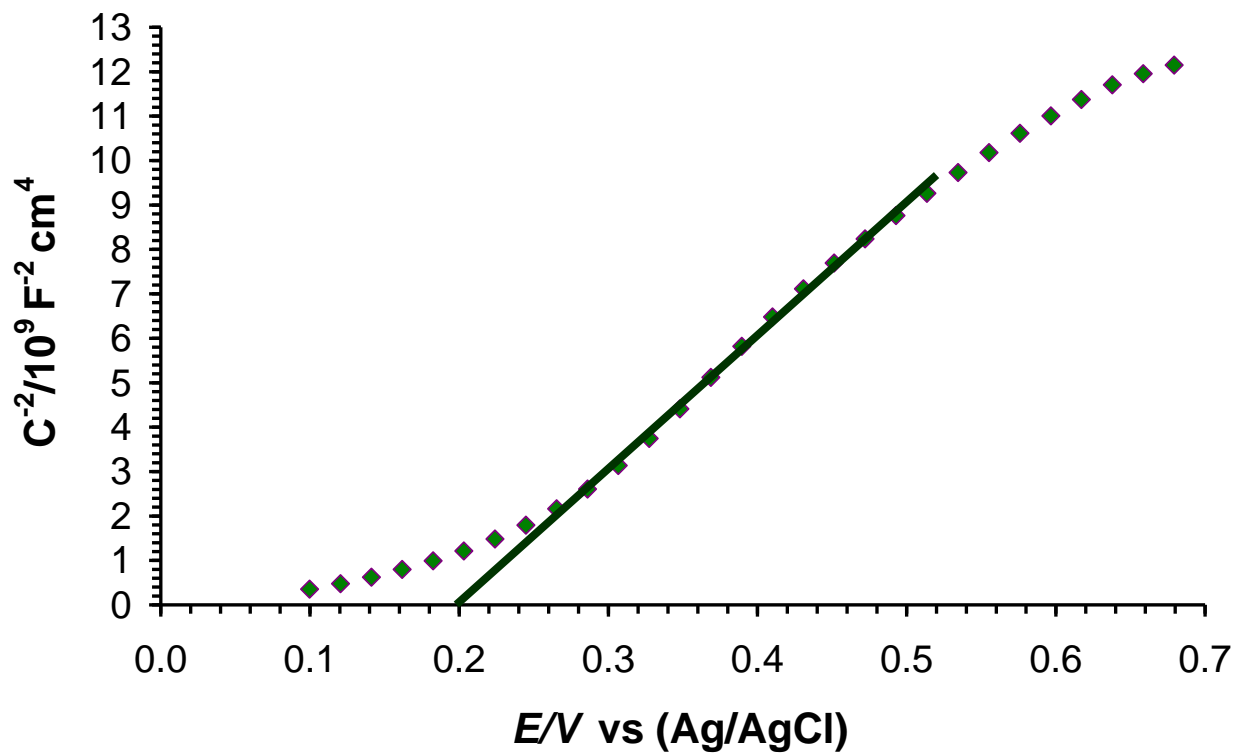


Figure 8

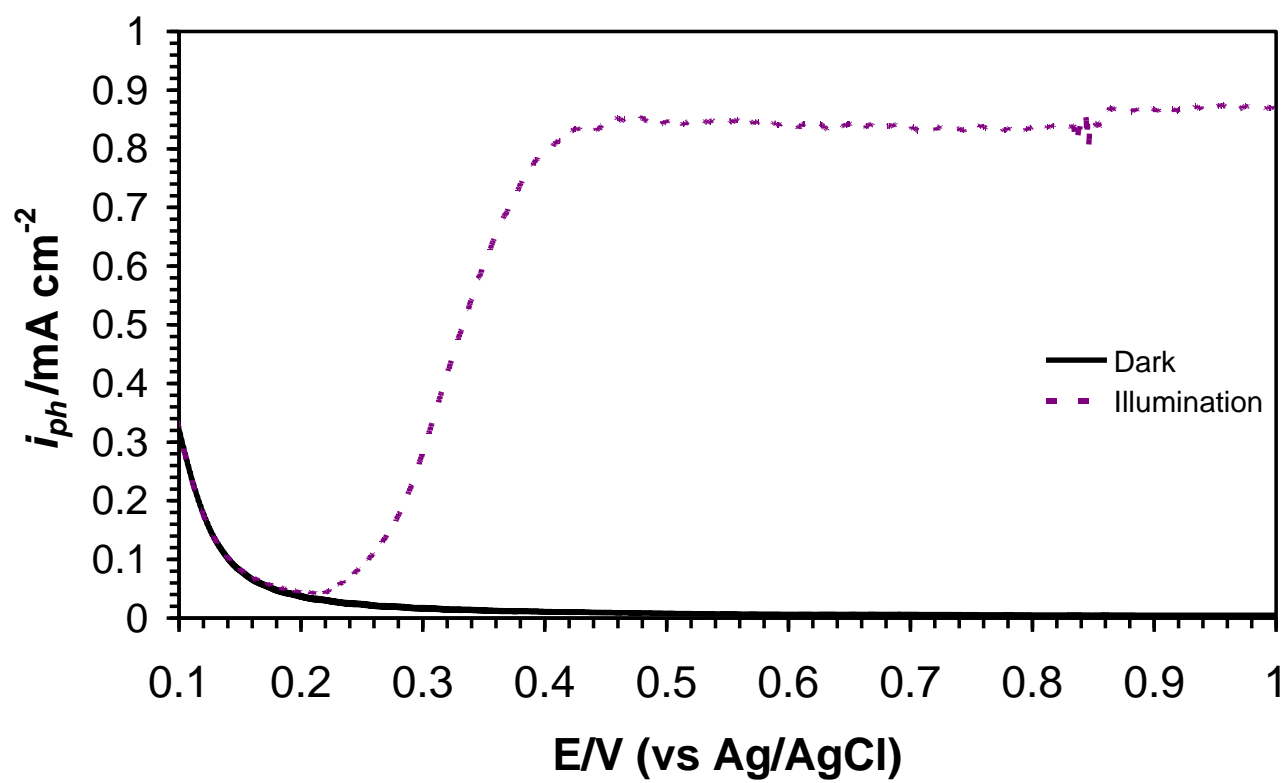


Figure 9

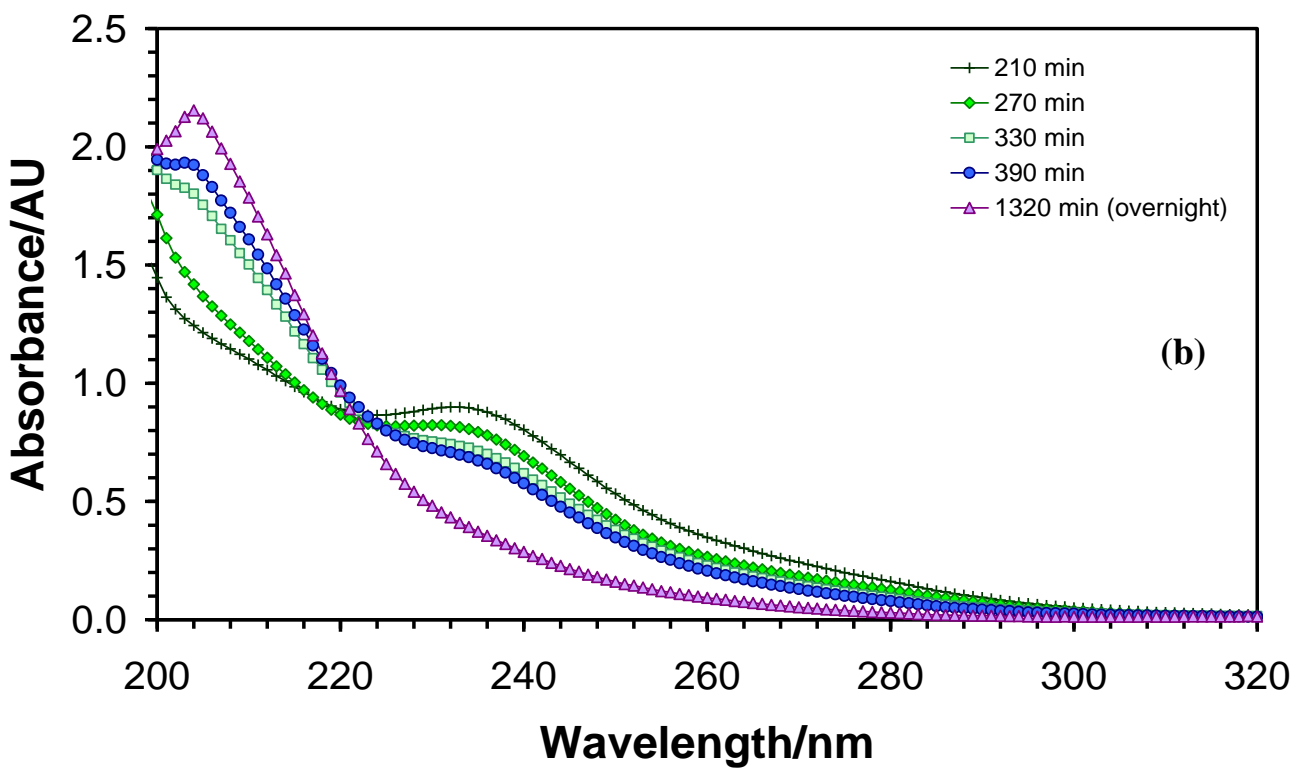
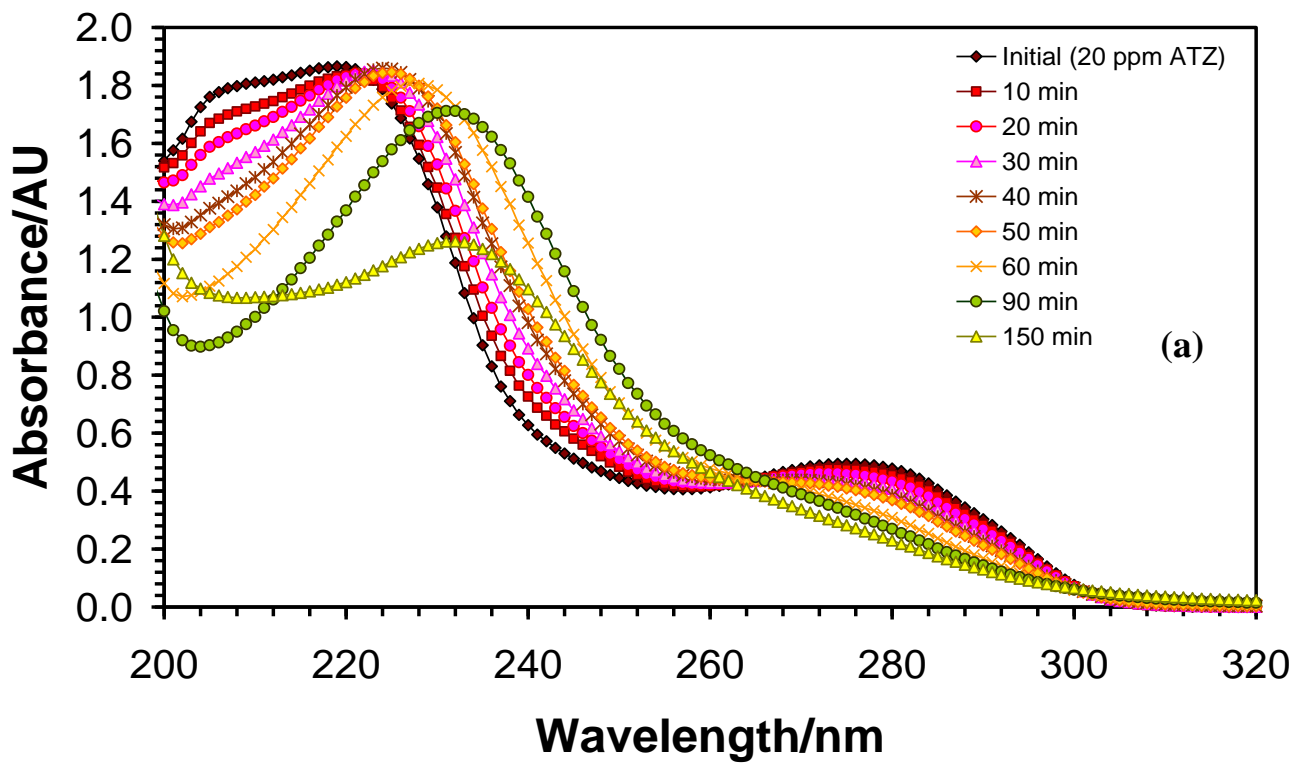


Figure 10

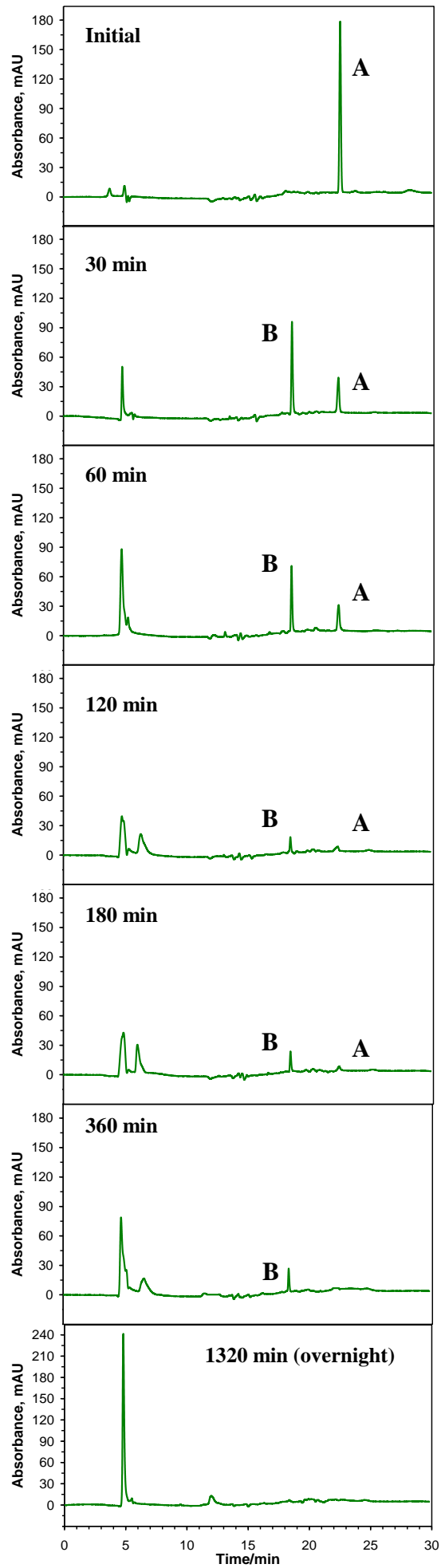


Figure 11

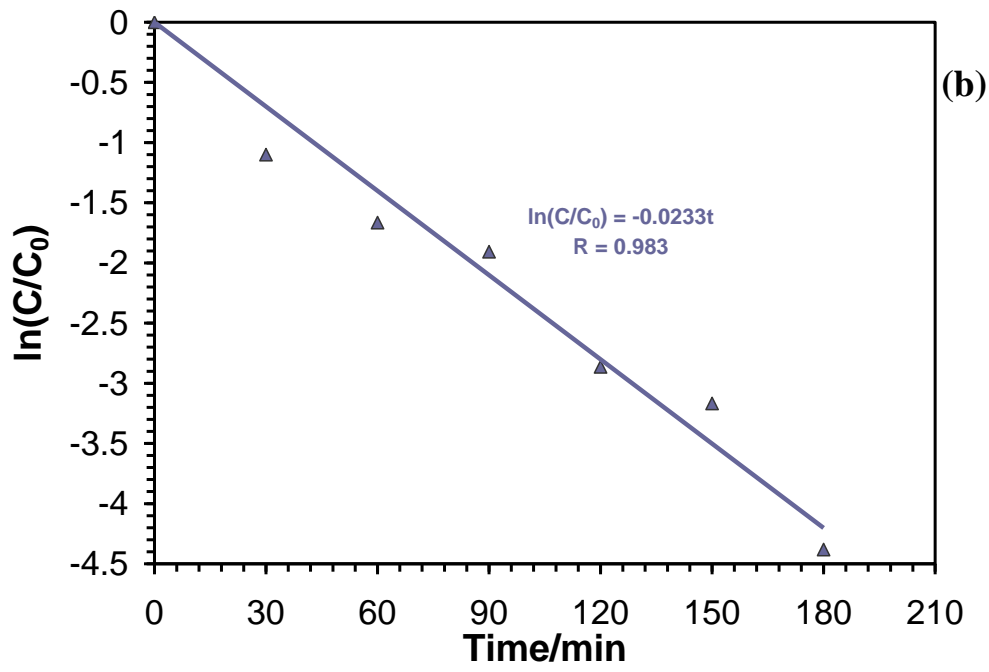
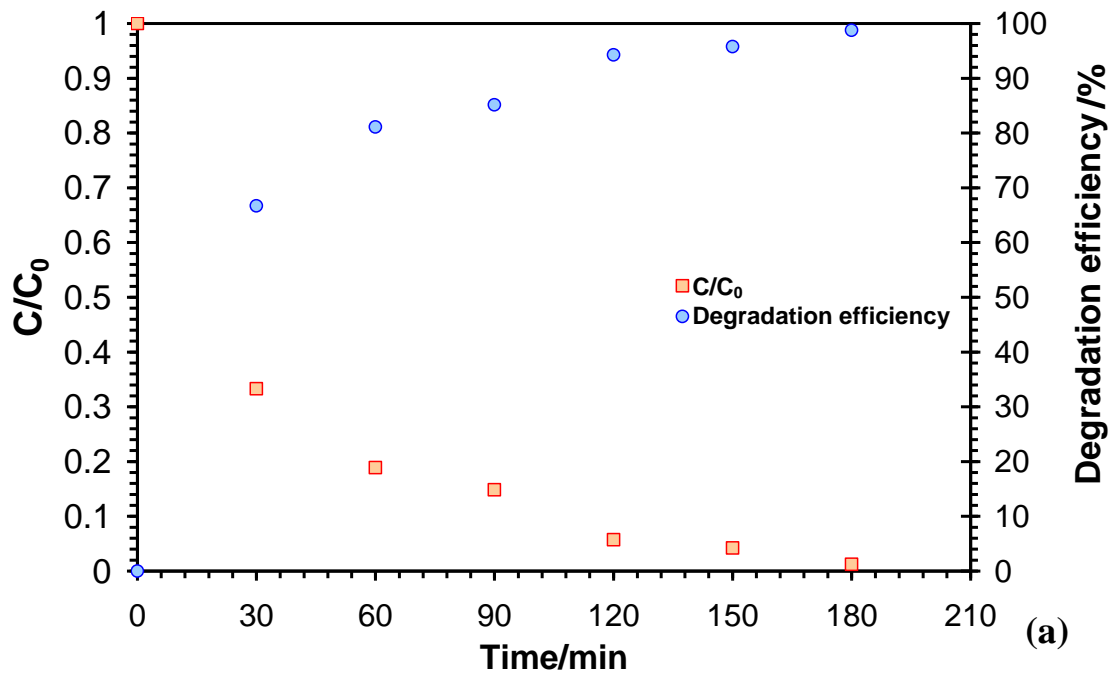


Figure 12

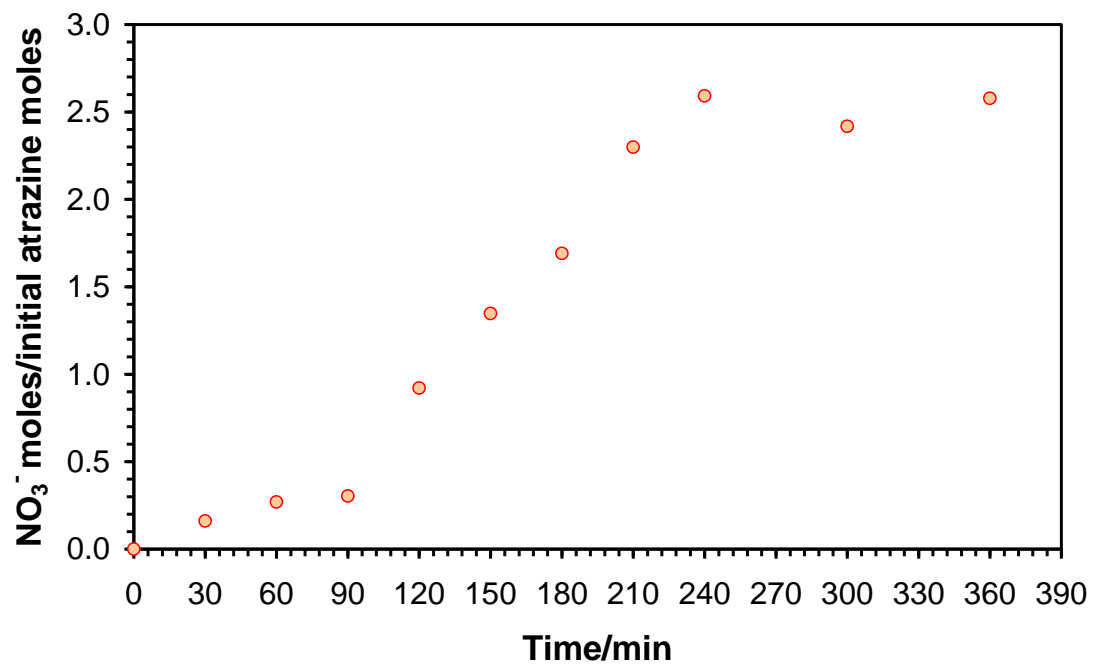


Figure 13

